Properties evolution of LaCoO₃ Perovskite synthesized by reactive grinding - Application to the toluene oxidation reaction

Bertrand Heidinger, Sebastien Royer, Jean-Marc Giraudon, Pardis Simon, Nicolas Bion, H. Alamdari, Jean-Francois Lamonier

Journal of Environmental Chemical Engineering 12 (2024) 112107

Contents lists available at ScienceDirect

Journal of Environmental Chemical Engineering

journal homepage: www.elsevier.com/locate/jece

Properties evolution of $LaCoO_3$ Perovskite synthesized by reactive grinding – Application to the toluene oxidation reaction

Bertrand Heidinger [a,b], Sébastien Royer [a], Jean-Marc Giraudon [a], Pardis Simon [a], Nicolas Bion [c], Houshang Alamdari [b], Jean-François Lamonier [a,*]

[a] Univ. Lille, CNRS, Centrale Lille, Univ. Artois, UMR 8181, UCCS, Unité de Catalyse et Chimie du Solide, F-59000 Lille, France
[b] Department of Mining. Metallurgical and Materials Engineering, Université Laval, Québec G1V 0A6, Canada
[c] Institut de Chimie des Milieux et Matériaux de Poitiers (IC2MP), Université de Poitiers-CNRS, 4 rue Michel Brunet, TSA51106, Cedex 9, F-86073 Poitiers, France

ARTICLE INFO

Editor: Kaimin Shih

Keywords:
Perovskite
Reactive grinding
Catalytic oxidation
Volatile organic compounds
Toluene

ABSTRACT

Perovskites are well known materials that are considered as viable alternative to noble metal-based catalysts in the environmental field. To be competitive, major issues such as unattractive textural properties and lower intrinsic activities than those of noble metal counterparts must be first addressed. On the other hand, reactive grinding is a versatile method to efficiently synthesize materials with improved textural properties, depending on the sequence and parameters. $LaCoO_3$ perovskites were synthesized by a three-step reactive grinding top-down process: (i) solid-state reaction – SSR; (ii) high energy ball milling – HEBM; (iii) low energy ball milling – LEBM. The physicochemical properties evolution of perovskite materials over the reactive grinding process was investigated by XRD, N_2-physisorption, ICP-OES, XPS, H_2-TPR, O_2-TPD and OIE, while their catalytic performances were evaluated for the toluene total oxidation reaction in dry and wet conditions. Each successive reactive grinding step allowed us to optimize the catalysts textural properties, with respectively the obtention of a microcrystalline material, a drastic reduction of crystal size to a nanometric scale along with formation of dense particles and then a significant increase of specific surface area up to 50 $m^2 \cdot g^{-1}$ by particles deagglomeration. The reactive grinding sequence presented here also deeply impacted the redox properties of $LaCoO_3$ catalysts, leading to increased performances in the toluene total oxidation reaction (SSR < HEBM < LEBM). A special care was paid to the impact of Fe contamination over grinding steps and time, on redox and catalytic properties of $LaCoO_3$ samples.

1. Introduction

Major endeavors have been done in the last decades to improve air quality, pushed by stringent environmental regulations [1,2] but the industry sector is still a significant contributor to volatile organic compounds (VOCs) emissions, which are responsible of important impact on health and environment. Toluene, being part of the BTX family with benzene and xylene compounds, is widely used in industry processes, such as an organic solvent, synthesis precursor, cleaning agent or even fuel additive [3]. Toluene, especially when mixed with benzene, has been recognized as potential carcinogenic, mutagenic and reprotoxic (CMR) substance [4], possesses consequent greenhouse power and participates to the formation of photochemical smog and ozone by atmospheric photoreactions [5,6]. Thus, professional exposure limits have been proposed to protect workers, with a long- and short-term threshold limit values (TLV) respectively set at 50 and 100 ppmv for the European Union [7]. Hazardous chemical substitution is highly encouraged but the cost and the difficulties to adapt already well-optimized industrial processes make post-treatment solutions an easier immediate choice. Among them, catalytic oxidation processes exhibit attractive characteristics with a limited energy consumption and a complete and selective elimination of pollutants [8]. Contribution to cleaner production from the point of view of VOC emissions abatement has been recently reviewed [9]. This review discussed the mechanism and current advancement of non-noble metal catalysts to remove VOCs and underlined the potentiality of perovskites materials as catalyst. ABO_3 Perovskite-type mixed oxides are a well-known class of materials due to a large variety of physical and chemical properties based on A and B atoms association, making them candidate for numerous applications including in the field of heterogeneous catalysis [10,11]. Often

* Corresponding author.
E-mail address: jean-francois.lamonier@univ-lille.fr (J.-F. Lamonier).

https://doi.org/10.1016/j.jece.2024.112107
Received 1 June 2023; Received in revised form 7 January 2024; Accepted 30 January 2024
Available online 1 February 2024

considered as a promising alternative to precious metal-based catalysts, perovskite-type materials exhibit interesting catalytic activities and stabilities for VOCs oxidation [12–14] while constituting elements being cheaper and more available than platinoid group metals (PGM) [15]. However, perovskites are generally presenting significantly lower activity than optimized supported noble metals, one of the reasons being the limited textural properties achieved with the classical synthesis procedures that represent a major technical limitation, hence reduce their appeal to a practical use. Indeed, the synthesis method has a huge impact on perovskite properties [16–18] and key factors such as transition metal surface accessibility, specific surface area and crystal domain size; all three of them having an important effect on cation reducibility and thus on catalytic activity, should be optimized.

Solution-mediated synthesis routes allow the production of material with good textural properties, suitable for a catalytic application [18–20], at the cost of a significant amount of solvent, steps and/or thermal energy, that lower the benefits for a pollutant remediation aim. For example, citrate-based synthesis the reference synthesis procedure originally proposed by Courty et al. [21], requires the use of citric acid (1 mol of citric acid per mole of NO_3^- from the nitrate precursor) in addition to hundreds of milliliters of water per gram of perovskite. Decomposition of the precursor results in the production of a significant stoichiometric amount of CO_2 and NOx. However, this method can achieve satisfactory surface areas, generally between 10 and 20 $m^2.g^{-1}$ [12,13], resulting in high-performance materials compared with solid-state ceramic solids. More sophisticated methods have even been proposed such as hard templating [13], microemulsion [13] and electrospinning [22].

On the other hand, reactive grinding (RG) process is a versatile approach commonly used in metallurgy that offers attractive features such as flexibility, limited use of solvents, atmospheric pressure and low temperature of synthesis [23,24]. Grinding processes are also commonly used in the industry, making the approach easily scalable. Early reports of RG-synthesized perovskites implied extended grinding times and/or the addition of porogenic compounds to get access to suitable catalysts [25–27]. The association of different grindings steps and parameters allows the design of a reactive grinding sequence based on the desired properties of final product, and many efforts were done to increase both economic and ecofriendly factors. Thus, the method has shown its potential to efficiently produce materials with finely tuned textural properties, such as MnO_2, several perovskite- and hexaaluminates-based catalysts [28–30]. The catalytic activity of perovskites depends on the nature of the transition metal, and cobalt is one of the most efficient transition metals for the total oxidation of VOCs. The catalytic activity of $LaCoO_3$ in toluene oxidation has been investigated by various authors using different approaches for catalyst preparation by studying the effect of Co^{3+} spin states [31], the influence of acid treatment [32] or the impact of A-site non-stoichiometry [33]. In the present work, $LaCoO_3$ perovskite-type mixed oxide are obtained by a three-step reactive grinding top-down process. The selected sequence is constituted of: (i) a solid-state reaction in order to obtain a well crystallized perovskite phase from the respective single oxides, followed by structural and textural modifications with (ii) a high energy ball milling (HEBM) step for crystal size reduction and (iii) a low energy ball milling (LEBM) step for surface area development. Solids are characterized at each step of the synthesis to investigate the impact of reactive grinding steps over the chemical and physical properties, as well as catalytic performances in both dry and wet conditions for the toluene total oxidation reaction.

2. Material and methods

2.1. Synthesis

Perovskite-type mixed metal oxides $LaCoO_3$ were synthesized by a three-steps reactive grinding process. Advantages associated to this method are: a limited amount of solvent used, an easy scalability and excellent reproducibility, a high versatility being adaptable to materials of various nature [24]. Step 1 consists in a classical Solid State Reaction (SSR; also commonly called ceramic method): oxide precursors (La_2O_3 and Co_3O_4) were homogeneously mixed at a molar La:Co ratio equal to 1.0. Obtained powder is calcined for 4 h at 1100 °C under static air atmosphere to obtain the perovskite phase, a temperature enough to allow the crystallization of the perovskite phase. In step 2, HEBM step is performed. Mass of SSR sample used for each LEBM step is 9 g per batch. Milling was performed for 90 min using a SPEX 8000D grinder with stainless steel equipment and balls (ø 1×11 mm. 2 ×12.5 mm) under static air atmosphere, at a revolution frequency of 17.5 Hz (1060 cycle·min^{-1}). The step 3 consists in the Low Energy Ball Milling (LEBM). LEBM is conducted with 60 g of HEBM sample. Milling was performed for different times up to 480 min using a Union Process Svegvari attritor with stainless steel equipment and balls (ø 5 mm), with addition of a small amount of water (0.4 mL per g of material) and operated at a rotation speed of 450 rpm. The milled sample was recovered using 100 mL of water (or 500 mL for two selected samples, marked with a *) and dried at 150 °C overnight. All materials were calcined for 3 h at 400 °C prior to characterization and catalytic performance evaluation. Pt/Al_2O_3 reference catalyst was synthesized by Incipient Wetness Impregnation method (IWI). The appropriate amount to obtain 0.5% Pt loading of the precursor K_2PtCl_6 (Fisher chemical) was dissolved in water (volume adjusted to the pore volume of Al_2O_3). The aqueous solution of the precursor was mixed with the support, then dried first at room temperature for 24 h in the dark, then at 180 °C for 24 h. The solid was then calcined at 500 °C for 5 h in order to obtain the reference catalyst denoted $0.5Pt/Al_2O_3$.

2.2. Physico-chemical characterizations

Diffractograms were recorded on a Bruker D8 apparatus, using Cu Kα radiation (λ = 1.54059 Å). Data were collected for 2θ between 10° and 80°, with an increment of 0.05° and an integration time of 1.0 s at each step. Diffractograms were indexed using references powder diffraction file (PDF) database. Crystallite mean sizes are calculated using the Scherrer equation: $D_{cryst} = (k \cdot \lambda)/(\beta \cdot \cos\theta)$, where k and β are respectively the shape factor (~0.9) and the corrected full width at half maximum of the single reflection peaks located at 2θ= 23.1 and 47.4°. High temperature diffractograms are recorded on a Bruker D8 apparatus coupled to an Anton Paar XRK900 reaction cell. A known mass of catalyst, taken from the first synthesis step (*i.e.* solid-state reaction), was heated under reductive conditions (similar to temperature programmed reduction (TPR) experiments) and data acquisition conditions are the same than X-ray diffraction (XRD) proceeded at ambient temperature. Scanning electron microscopy (SEM) characterization was performed using a JEOL microscope model JSM 5300. Prior to SEM analysis, a thin carbon coating was deposited on the samples. N_2-physisorption experiments were collected on a Micromeritics Tristar II porosity instrument. A known mass of catalyst was degassed at 150 °C under vacuum for 6 h. Isotherms were registered at a temperature of − 196 °C and specific surface area (SSA) were determined from the adsorption branch in the 0.05–0.30 P/P_0 range with the Brunauer-Emmett-Teller equation (BET). Inductively coupled plasma optical emission spectroscopy (ICP-OES) measures were done on an Agilent 5110 apparatus. Before analysis, a known mass of sample was mineralized in strongly acidic solution, passed through a 0.45 μm filter and diluted by a 2% factor. H_2 -TPR experiments were performed on a Micromeritics AutoChem II 2920 chemisorption analyzer. A catalyst mass fixed to ~40 mg was inserted in a quartz reactor and degassed under inert gas. A flow of 5 vol% H_2/N_2 was stabilized at a total flow rate of 50 mL·min^{-1} and the catalyst was heated from 40 °C to 1000 °C at a temperature increase rate of 10 °C·min^{-1} (experimental K and P parameters respectively of 88 s and 15 °C). O_2-Temperature Programmed Desorption (O_2-TPD) experiments were carried out with the same instrument. A sample mass of ~100 mg was pretreated under synthetic air at a flow rate of 20 mL min^{-1} at

400 °C (temperature increase rate of 10 °C min^{-1}) for 2 h before being cooled to room temperature under air flow. Then the material is flushed under an inert gas flow (He, 30 mL min^{-1}) for 40 min. Desorption was carried out from room temperature to 1000 °C under He flow (30 mL min^{-1}) at a heating rate of 10 °C min^{-1}. The gas flow at the reactor outlet is analyzed using a thermal conductivity detector (TCD) and a mass spectrometer ($m/z = 32$, O_2; $m/z = 18$, H_2O; $m/z = 28$, N_2; $m/z = 44$, CO_2). Oxygen isotope exchange (OIE) experiments were performed on a recirculation-type tubular reactor. A sample mass of 20 mg was inserted in a quartz reaction cell, calcined at 400 °C for 1 h under pure $^{16}O_2$ atmosphere (flow rate: 50 mL·min^{-1}) and degassed under vacuum for 30 min at a temperature of 400 °C. The system is then stabilized and a pressure of 55 mbar of $^{18}O_2$ is applied. Partial pressures evolution is monitored using mass spectrometry ($^{16}O_2$, $m/z = 32$; $^{18}O^{16}O$, $m/z = 34$; $^{18}O_2$, $m/z = 36$; N_2, $m/z = 28$). X-ray photoelectron spectroscopy (XPS) analysis was carried out using a Kratos AXIS Ultra DLD apparatus with a monochromated Al Kα (1486.7 eV) source working at 225 W (15 mA, 15 kV). La 3d, Co 2p, O1s, and C1s core level spectra as well as Fe 2p energy region were acquired with a Pass Energy 20 eV. Processing was performed using CasaXPS software, spectra being energy-corrected according to the main C 1 s peak positioned at 284.8 eV. Quantification results are based on the La 3d, O 1 s and Co 2p peak areas after a Shirley type background subtraction.

2.3. Catalytic activity measurements

Catalytic performances were evaluated in the gas phase toluene oxidation reaction. A mass of catalyst equal to 0.200 g was positioned in a fixed bed reactor and was heated from 25 °C to 330 °C for 30 min (2 °C·min^{-1}) under synthetic air flow. Then, the reaction flow, composed of 1000 ppmv of toluene diluted in synthetic air, was stabilized at a flow rate of 100 mL·min^{-1} (given a WHSV = 30,000 mL·h^{-1}·g^{-1}) and the reactor temperature was allowed to decrease from 300 °C to 150 °C at a constant temperature decrease rate of −0.5 °C·min^{-1}. Stability experiments were performed during 70 h and 100 h at a constant temperature of 220 °C and 230 °C, respectively. The off-gases were analyzed on-line using a gas chromatograph (μGC, R3000 Agilent Gas Chromatograph) equipped with a thermal conductivity detector (TCD) using a Stabilwax (10 m) column. The results were expressed in terms of toluene conversion into carbon dioxide: $X(\%) = 100 \cdot [CO_2]_{out}/(7 \cdot [C_7H_8]_{in})$. Corrected pre-exponential factors ($A_{0\ corr}$) have been recalculated considering an average activation energy (Ea) of 159 kJ·mol^{-1}. To quantify the resistance against deactivation, an activity coefficient a_{220} was defined as the ratio between the toluene conversion after 70 h reaction to that at the initial time. To mimic real conditions, catalytic performances were also evaluated in wet conditions, adding a water quantity to the gas stream corresponding to a relative humidity (RH) at 20 °C of 25%, 50% and 75%.

3. Results and discussion

3.1. Physico-chemical characterization

X-ray diffractograms obtained for $LaCoO_3$ materials at different stages of the reactive grinding process are shown in Fig. 1. In the case of SSR sample, diffractogram exhibits intense and narrow peaks that matches with the $LaCoO_3$ reference compound of R3c rhombohedral structure (JCPDS #48–0123), which indicates the formation of a microcrystalline sample. In addition to the $LaCoO_3$ perovskite phase, weak diffraction peaks are observed (2θ = 27.3°, 28.0°, 39.5°, 48.3°, 48.6° et 64.0°) that corresponds to a lanthanum hydroxide $La(OH)_3$ secondary phase (JCPDS #36–1481), resulting from an unreacted fraction of lanthanum oxide (La_2O_3) precursor. Indeed, in air, La_2O_3 hydrates easily to form $La(OH)_3$ together with lanthanum carbonates (when in the presence of CO_2). Therefore, the presence of $La(OH)_3$, visible as very weak signals in the diffraction pattern of SSR, is

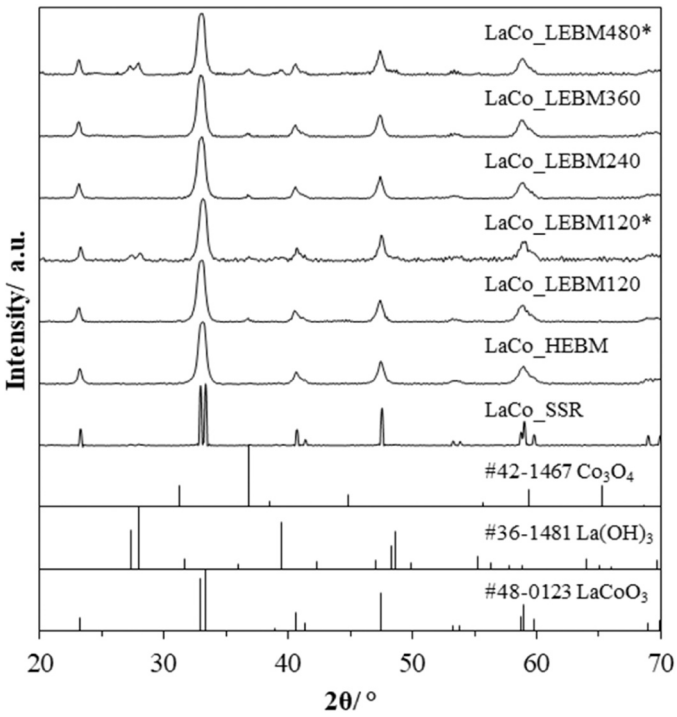

Fig. 1. Diffractograms of $LaCoO_3$ samples at the different steps of reactive grinding process. SSR, solid state reaction; HEBM, high energy ball milling; LEBM, low energy ball milling. Bottom of the figure: vertical bars are for cited JCPDS references.

associated to the hydration of external – unreacted – La_2O_3. Diffractogram of the HEBM sample still exhibits $LaCoO_3$ phase characteristic diffraction peaks, therefore perovskite structure is maintained during high energy ball milling process. One can observe that diffraction peaks are significantly weaker in intensity with larger full width at half maximum value (FWHM). This shape change results from an important crystallite size reduction due to their fractioning while being milled at high energy [30,34]. Diffraction peaks relative to the $La(OH)_3$ secondary phase is no more present. It can be explained either by reaction completion during HEBM process, which is able to bring sufficient energy to the system to achieve the $LaCoO_3$ formation, either by dispersing and homogenizing $La(OH)_3$ phase into the perovskite sample, or either a combination of both. Diffractograms obtained for LEBM $LaCoO_3$ samples are quite identical, regardless of low energy grinding time, and no noticeable structural change is observed in comparison to the LaCo_HEBM sample one. However, a weak but constant in intensity reflection peak has appeared at 2θ = 36.9° that corresponds to a cobalt oxide secondary phase (Co_3O_4; JCPDS #42–1467).

Both LaCo_LEBM120 * and LaCo_LEBM480 * samples, which had received different treatment in comparison to unmarked samples (500 mL of water for material recovery instead of 100 mL), exhibit diffractogram having the previously described components plus weak additional diffraction peaks corresponding to a lanthanum hydroxide secondary phase $La(OH)_3$ (JCPDS #36–1481). It is worth mentioning that the Co_3O_4 diffraction peak (2θ = 36.9°) seems to be slightly more intense than for unmarked samples.

Crystallites mean size was estimated applying the Scherrer equation on the 2θ = 23.2° et 47.5° diffraction peaks (Table 1). While LaCo_SSR sample crystallites are larger than what can be estimated by the Scherrer equation (>80 nm), LaCo_HEBM sample presents strongly reduced crystallites mean size (12 nm). No further evolution is observed for LEBM samples. These values agree with $LaCoO_3$ perovskites ones analogously synthesized by Royer *et al.* [17]. Indeed, comparable crystallite sizes has been reported for the ceramic material (74 nm) and for the

Table 1
Structural textural properties and elemental composition obtained for $LaCoO_3$ samples at different steps of reactive grinding process.

Sample	Phase (s)	D_{cryst} (nm)	SSA[b] ($m^b \cdot g^{-a}$)	Fe cont.[c] (at%)
LaCo_SSR	P. $La(OH)_3$	> 500[a]	< 1.0	0.3
LaCo_HEBM	P	12	3.5	0.7
LaCo_LEBM30	P. Co_3O_4	11	6	1.4
LaCo_LEBM60	P. Co_3O_4	12	7	1.7
LaCo_LEBM90	P. Co_3O_4	13	13	2.0
LaCo_LEBM120	P. Co_3O_4	11	21	2.3
LaCo_LEBM120 *	P. $La(OH)_3$. Co_3O_4	11	50	2.3
LaCo_LEBM180	P. Co_3O_4	12	29	n.d.
LaCo_LEBM240	P. Co_3O_4	13	30	n.d.
LaCo_LEBM360	P. Co_3O_4	11	36	n.d.
LaCo_LEBM480 *	P. $La(OH)_3$. Co_3O_4	13	52	n.d.

P: perovskite
[a] determined by SEM
[b] SSA: Specific surface area
[c] measured by ICP-OES;n.d.: non-determined

ground sample (16 nm after calcination at 550 °C) [17]. Compared with a more conventional synthesis, such as citrate complexation, the calcination step at ~ 600 °C required for crystallization induces crystal growth of up to 27 nm [17].

Morphology evolution of $LaCoO_3$ samples over reactive grinding process was monitored by SEM (Fig. 2). The LaCo_SSR sample is mostly composed of micrometric crystals that is consistent with materials issued from ceramic process and needed high temperature crystallization steps. HEBM step highly impacts sample morphology with only the presence of large and dense aggregates of nanometric crystallites. LEBM step shows a more limited impact on the sample morphology which is mostly similar to the HEBM sample one, nonetheless elementary particles are easier to discern thanks to progressive aggregate deagglomeration during low energy ball milling process. Finally, marked sample case is investigated (LaCo_LEBM120 *, Fig. 2(d)). The sample picture radically differs from the previous ones, with sheet- and needle-like elements that are respectively attributed to $La(OH)_3$ and Co_3O_4 secondary phases observed on diffractogram (Fig. 1).

LaCo_SSR sample SSA is quite low (< 1.0 $m^2 \cdot g^{-1}$) which is in agreement with surfaces reported for material produced by ceramic process. While LaCo_HEBM sample shows a slightly higher SSA value (< 3.5 $m^2 \cdot g^{-1}$), the value does not reflect the drastic crystallite reduction size and results from the highly aggregated state of the sample (Fig. 2(a-b)). The low surface areas displayed by the perovskite, even after grinding, are associated to the aggregate-like porosity associated [29] to the nanoparticle size that remains relatively large (>10 nm) and the intra-aggregate porosity contraction during thermal treatment [17].

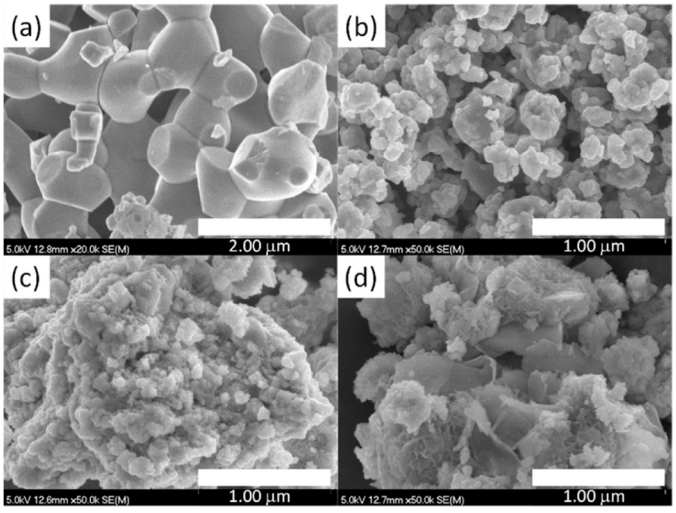

Fig. 2. Scanning electron microscope (SEM) images obtained for (a) LaCo_SSR, (b) LaCo_HEBM, (c) LaCo_LEBM90 and (d) LaCo_LEBM120 * samples, taken after calcination step (400 °C). Magnification: (a), 20x; (b–d), 50x.

SSA evolution as a function of LEBM grinding time, for as made samples and their calcined counterpart, is presented in Fig. 3(A). A theoretical maximum SSA value of 69 $m^2 \cdot g^{-1}$ can be determined considering spherical shape particles, a density of 7.29 and a crystallite average size of 12 nm. From as made samples set, SSA value linearly increases with time until it reaches a maximum value of ~50 $m^2 \cdot g^{-1}$ and then stabilizes at $t \geq 180$ min. This value is smaller than the theoretical one, which results from a deagglomeration process that cannot be fully achieved. The difference between both values is attributed to residual grain boundaries and/or interparticle contacts. Marked LaCo_LEBM120 * et LaCo_LEBM480 * samples show much higher SSA values, with respectively 74 et 77 $m^2 \cdot g^{-1}$. That is explained by $La(OH)_3$ and Co_3O_4 secondary phases contribution to $LaCoO_3$ SSA (Fig. 1). SSA values of calcined samples show a similar trend that their as made counterparts.

Impact of calcination temperature upon SSA was investigated using LaCo_LEBM180 sample (Fig. 3(B)). As made LaCo_LEBM180 sample exhibits a SSA value of ~50 $m^2 \cdot g^{-1}$. A slight decrease is observed until a temperature of 400 °C, then a major SSA drop occurs in the 400–500 °C range. The SSA gain from LEBM process is lost when calcination temperature ≥ 700 °C is applied, with values of SSA being below 3.5 $m^2 \cdot g^{-1}$. Considering that toluene catalytic oxidation can be achieved at moderate temperature [17,18,35], calcination temperature can be set to 400 °C, a good compromise to retain attractive SSA.

As a consequence of LEBM step is possible contamination by the elements the milling parts are composed of, since these parts can be in contact with the sample for extended times [26,28,29]. Such contamination, especially with iron, has been reported having a negative impact upon catalytic performances [17,28]. Iron contamination has been monitored for early reactive grinding synthesis stages (Table 1). LaCo_SSR and LaCo_HEBM samples present low iron contamination value, whereas LaCo_LEBM samples see their iron level increased by a larger amount (Table 1), which is explained by a greater surface contact between material and grinding elements (*i.e.* steel balls). Interestingly, the increase of Fe amount brought during LEBM process increase linearly with time (Fig. 3(C)).

$LaCoO_3$ samples surface chemistry was probed using XPS. Quantification results, based on La 3d, Co 2p and O 1 s peak areas, are shown in Table A.1. One can see that La/Co atomic ratio is higher than 1.0 for each $LaCoO_3$ sample with values ranging from 1.47 to 1.82. Such surface La enrichment is frequently reported for perovskite-type compounds and is bound to the ability of surface lanthanum to react with moisty or CO_2 to form hydroxy and/or carbonate surface species [36–38]. While La surface concentration tends to decrease linearly with time during LEBM process, Co surface concentration follows an opposite trend, getting a La/Co atomic ratio near stoichiometry at extended grinding times (*e.g.* LaCo_LEBM360).

Satisfying peak fitting of Oxygen O 1 s core level spectra can be achieved with three components (Fig. 4(A)): The O_I component at low binding energy (BE= 528.9 eV) assigned to lattice oxygen (O^{2-}) [39]; the O_{II} component at intermediate binding energy (531.2 eV) corresponding to several surface species such as O^-, O_2^{2-}, HO^- and/or CO_3^{2-} [38]; the O_{III} component at high binding energy (533.3 eV) associated to adsorbed H_2O [40]. A noticeable decrease of O_{II} component is observed after HEBM step, which can be correlated to the disappearance of $La(OH)_3$ surface species in the high energy milling process (Fig. 1). Unlike to our previous results [29], O_{II} component tends to increase back during LEBM process. This can be linked to the CO_3^{2-} component observed on C 1 s signal (Fig. 4(B)).

In addition to O 1 s and C 1 s, were monitored cobalt and iron with respectively Co 2p and Fe 2p photopeaks (Fig. A1). $LaCoO_3$ samples show a very similar Co 2p signature for all samples that indicates no major modification of Co chemical state while being milled (Fig. A1(A)).

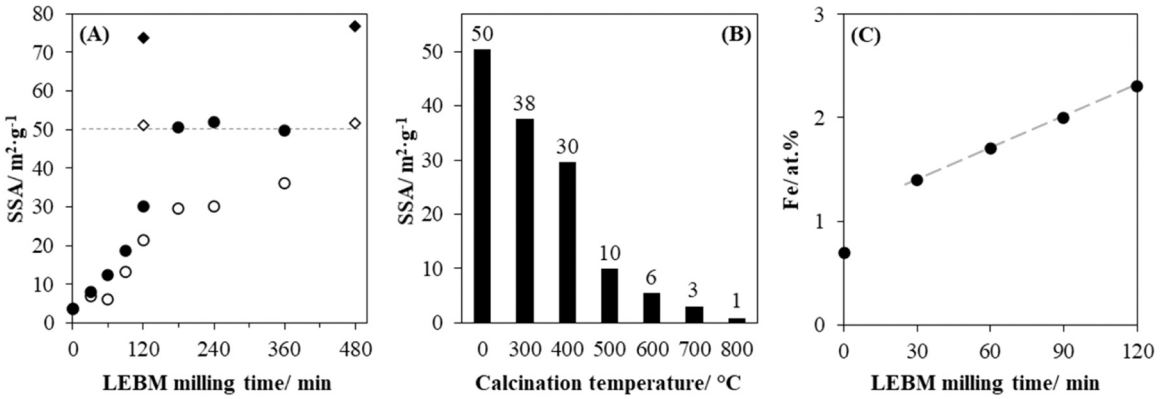

Fig. 3. (A) SSA evolution as a function of low energy ball milling (LEBM) grinding time (full symbols) and SSA of calcined (400 °C) corresponding samples (open symbols). ◆ and ◊ refer to marked samples (*i.e.* LEBM120 *. LEBM480 *). (B) SSA evolution of LaCo_LEBM180 sample as a function of calcination temperature. (C) Fe contamination evolution as a function of low energy ball milling (LEBM) grinding time.

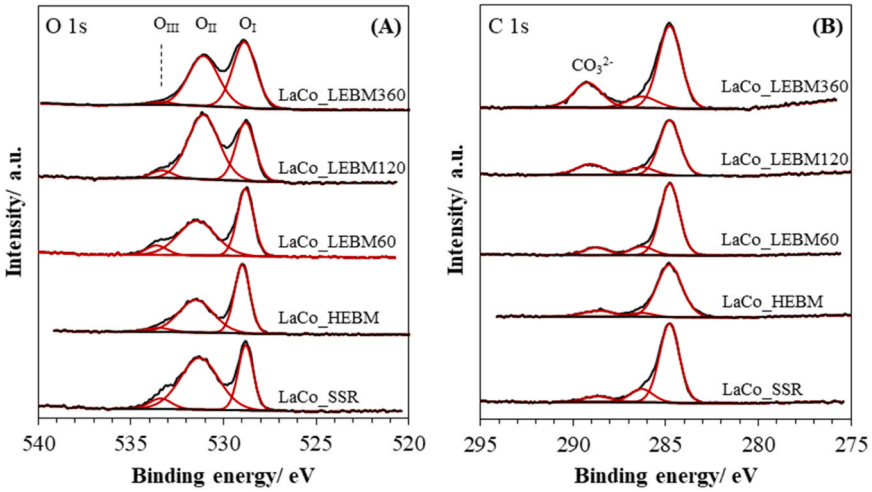

Fig. 4. High resolution spectra of the **(A)** O 1 s and **(B)** C 1 s core level spectra for $LaCoO_3$ samples. SSR, solid state reaction; HEBM, high energy ball milling; LEBM, low energy ball milling.

Co 2p photopeaks can be curve-fitted with a main peak centered at 779.8 eV alongside two multiplet peaks and a satellite peak (789.8 eV), which is identified as Co^{3+} species [41–43]. The absence of a second satellite at 785.9 eV, characteristic of Co^{2+} species, indicates that surface cobalt is only under Co(+III) form. While Fe concentration is quite low as determined by ICP-OES (Table 1), interference from Fe Auger peak (Fe LMM) was neglected in the Co 2p area. On the other hand, the Co Auger peak (Co LMM) interferes with the Fe 2p (Fig. A1(B)), thus exploitation should be handled with care [44]. The signal intensity increase at ~715 eV is imputed to the Co surface concentration over grinding processes (Table A.1). Nonetheless, a shoulder is easily observable at ~724 eV in $LaCoO_3$_LEBM360 sample which can be explained by electrons from Fe $2p_{1/2}$ level, if compared to the Fe 2p XPS spectra from a $LaFeO_3$ sample taken as reference [29].

Preliminary to in depth $LaCoO_3$ redox properties determination, LaCo_SSR phase evolution over temperature and under reductive atmosphere was monitored *in situ* (Fig. A2). The diffractogram taken at ambient temperature is identical to the one done in air condition (Fig. 1) with addition of Pt support peaks (2θ = 39.6° et 67.4°). This structural composition is maintained up to 400 °C, when cobalt reduction starts from Co(III) to Co(II) (*i.e.* $LaCoO_3$ → $La_3Co_3O_8$ (fiche JCPDS #89–1319)). The reduction continues at 500 °C $La_3Co_3O_8$ → $LaCoO_{2.5}$ (fiche JCPDS #04–008-6405)) and 600 °C with the appearance of La_2O_3 phase (2θ = 26.2°, 29.2°, 29.9°, 39.5°, 46.1°, 52.1°, 55.4°, 56.0° et 62.3°). Above a temperature of 700 °C, metallic cobalt Co^0 is observed (2θ = 44.3° and 51.7°).

H_2 Temperature-programmed reduction profiles are presented in Fig. 5 for selected samples. Then the reduction profiles and H_2-uptake evolution over temperature exhibit low temperature (LT, 200–500 °C) and high temperature (HT, 500–800 °C) reduction domains. This two steps process is identified to the successive reductions Co(III) → Co(+II), then Co(+II) → Co(0) [26,45,46], in accordance with *in situ* reduction followed by XRD (Fig. A2):

$$LaCoO_3 + \frac{1}{2}H_2 \longrightarrow LaCoO_{2.5} + \frac{1}{2}H_2O \quad (1)$$

$$LaCoO_{2.5} + H_2 \longrightarrow \frac{1}{2}La_2O_3 + Co^0 + H_2O \quad (2)$$

Iron species reduction, in the form of Fe_2O_3 or Fe^{3+} inserted in the perovskite crystal, occurs in the temperature range 250–500 °C [47]. It should therefore overlap with the Co(III) → Co(+II) reduction step, observed in Fig. 5. Considering the low iron content from grinder contamination (<2.3 at%, Table 1), and considering the limited level of iron reduction (Fe(III) → Fe(+II)), we assumed a negligible contribution of Fe reduction to the H_2 uptake.

LaCo_SSR sample reduction profile presents two reduction peaks in its LT domain. However, the first reduction process, *i.e.* below the sharp peak beginning above 600 °C, remains associated to the almost complete reduction of Co^{3+} from the sample (surface and bulk) into Co^{2+}, as

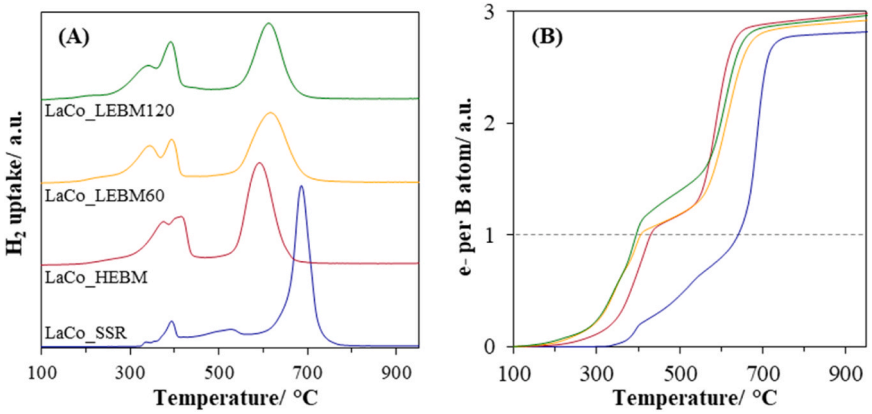

Fig. 5. (A) Temperature-programmed reduction (H_2-TPR) profiles and (B) cobalt reduction degree of $LaCoO_3$ samples.

confirmed by calculating the hydrogen consumption and comparing it to the total content needed to perform the Co^{3+} to Co^{2+} reduction (Fig. 5B). Indeed, the reduction level curve presented in Fig. 5(B) shows that a reduction of 0.8–0.85 e- (meaning 80–85% of the Co^{3+} will reduce to Co^{2+}) is achieved at the beginning of the reduction peak of the second step. The complete reduction of Co^{3+} to Co^{2+} is delayed when compared to the temperature at which the phenomenon occurs for nanocrystalline ground $LaCoO_3$, due to the bulk diffusion phenomenon occurring in large crystals [26,27]. Important modifications of the H_2-TPR profile are observed after HEBM process with an increase of H_2 consumption from LT domain and a global shift to lower temperatures. This reducibility increase is mainly explained by the crystallite mean size reduction (Table 1) [17]. Reduction profiles of LEBM samples are similar to the HEBM one, nonetheless an additional shift of the LT domain to lower temperature is observed, which is related to particle deagglomeration and SSA increase of $LaCoO_3$ samples during LEBM grinding [17]. Fig. 5 (B) present the level of reduction as a function of the reduction temperature. Reduction level is calculated from the cumulated hydrogen consumption at each point of the TPR, and taking into account of real Co content in the sample analyzed. Y-axis therefore presents the level of reduction of Co^{3+} to Co(0), knowing that cobalt, initially present as Co^{3+} in the oxidized perovskite, can reduce by 3 electrons to form metallic cobalt [17].

Electrons consumption per Co atom as a function of temperature show a consumption value higher than 1 for HEBM and LEBM samples in the LT domain (Fig. 5(B)) which indicate a fraction of cobalt reduced to metallic cobalt [48] which is clearly not the case for the SSR sample.

Cobalt atoms average oxidation state (AOS) in $LaCoO_3$ samples were estimated on the basis of H_2 uptake (Table A.2). AOS(Co) values are almost if not of 3, which is in accordance with the $LaCoO_3$ stoichiometry (Fig. 1) and XPS results (Fig. A1(A)).

Oxygen temperature-programmed desorption curves are presented Fig. 6. LaCo_SSR sample shows a unique and intense desorption peak centered at 911 °C. LaCo_HEBM and LaCo_LEBM60 samples a high temperature desorption peak shifted to lower temperature respectively by − 90 °C and − 79 °C. Two other desorption peaks are also observed at much lower temperature for these samples, with a maximum desorption at T = 220 °C and 450 °C for the LaCo_HEBM sample and T = 190 °C and 480 °C for the LaCo_LEBM60 one. The high temperature desorption peak is commonly attributed to lattice oxygen (β-O), whereas desorption peaks appearing at lower temperature are attributed to surface and grain boundaries oxygens (α-O) [11,49,50], which are weaker.

Desorbed oxygen quantification is reported in Table 2 on the desorption peak areas basis. Desorbed β-oxygen quantity depends on the synthesis method [17] and is indicative of the oxygen mobility into the bulk. The amount of oxygen desorbed at high temperature is in the same order for all three samples (~40 μmol·g^{-1}), which is comparable to $LaCoO_3$ system one obtained by Royer et al. using ceramic method,

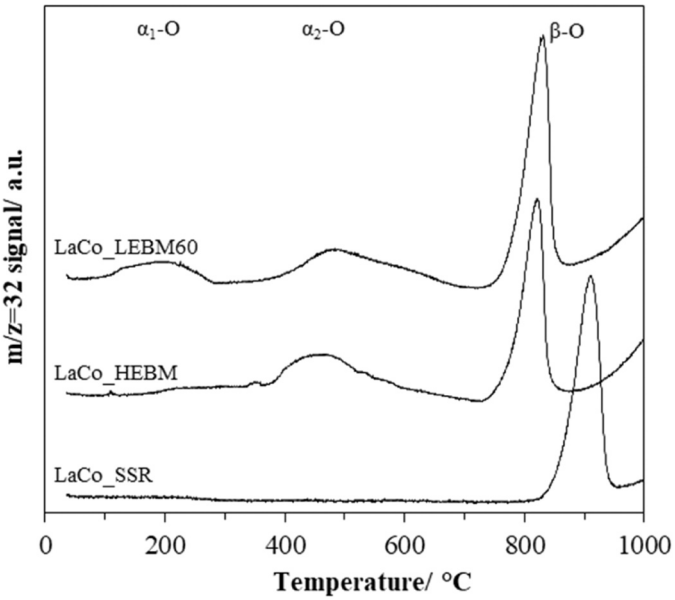

Fig. 6. O_2-TPD profiles ($m/z = 32$) of selected $LaCoO_3$ samples (ramp= +5 °C·min^{-1} under He).

Table 2
O_2-TPD results for $LaCoO_3$ samples.

Sample	Amount of Oxygen desorbed[a] (μmol·g^{-1})		Number of monolayer desorbed[b]	
	α	β	α	β
LaCo_SSR	–	43.0 (911)	–	17.9
LaCo_HEBM	11.6 (506)	35.8 (821)	0.83	2.6
LaCo_LEBM60	36.6 (482)	44.3 (832)	1.31	1.6

[a] corresponding T_{max} (°C) in parentheses;
[b] considering an amount of oxygen equal to 4.0 μmol·m^{-2} per monolayer.

whereas being smaller when others synthesis routes are used [17]. The three samples having a value very close despite grinding steps is explained by the shared first calcination step at high temperature (1100 °C). On the other hand, the value of desorbed α-oxygen increases significantly after each high and low energy ball milling step, while being close to ones of $LaCoO_3$ materials with comparable SSA [17]. In the case of either LaCo_HEBM or LaCo_LEBM60 sample, the value of β-oxygen desorbed normalized by unit of surface always corresponds to the desorption of more than one oxygen monolayer, as previously observed [17] which confirms the desorption of lattice oxygen at this

step.

In order to assess oxygen mobility evolution upon the different reactive grinding steps, oxygen isotopic exchange (OIE) isothermal curves are presented in Fig. 7. Experiments shows that oxygen exchange is set on a simple heteroexchange mechanism, which involves exchange of a unique ^{18}O atom with solid phase at a time, resulting in the simultaneous reduction of $^{18}O^{18}O$ fraction with augmentation of $^{18}O^{16}O$ fraction in the gas phase (Fig. 7(A)) [30] according to:

$$^{18}O^{18}O_{(g)} + {}^{16}O_{(s)} = {}^{18}O^{16}O_{(g)} + {}^{18}O_{(s)}$$

Oxygen mobility in $LaCoO_3$ materials is highly impacted by the origin of exchanged oxygen in the solid (surface > grain boundaries > structure) [51]. Consequently, OIE curves can be divided into two main domains characterized by: (i) a high exchange rate with the exchange of surface and grain boundaries type oxygens (t < 5 min); followed by (ii) a much lower exchange rate part corresponding to bulk oxygens (Fig. 7 (B)) [52].

$LaCoO_3$ samples IOE results are reported in Table 3. Initial exchange rate ($V_{e,ini}$), determined at t = 0 min, is minimal for the LaCo_SSR

Table 3
OIE results for $LaCoO_3$ samples.

Sample	Initial exchange rate ($V_{e,ini}$)[a] ($\times 10^{17}$ at·g^{-1}·s^{-1})	N_e[b] ($\times 10^{20}$ at·g^{-1})
LaCo_SSR	5.8 (-)	3.3
LaCo_HEBM	28.6 (8.2)	15.8
LaCo_LEBM60	121.3 (17.3)	18.4
LaCo_LEBM360	69.8 (1.9)	16.2

[a] corresponding value normalized with SSA in parentheses (at·s^{-1}·m^{-2});
[b] number of oxygen atoms exchanged at t = 60 min

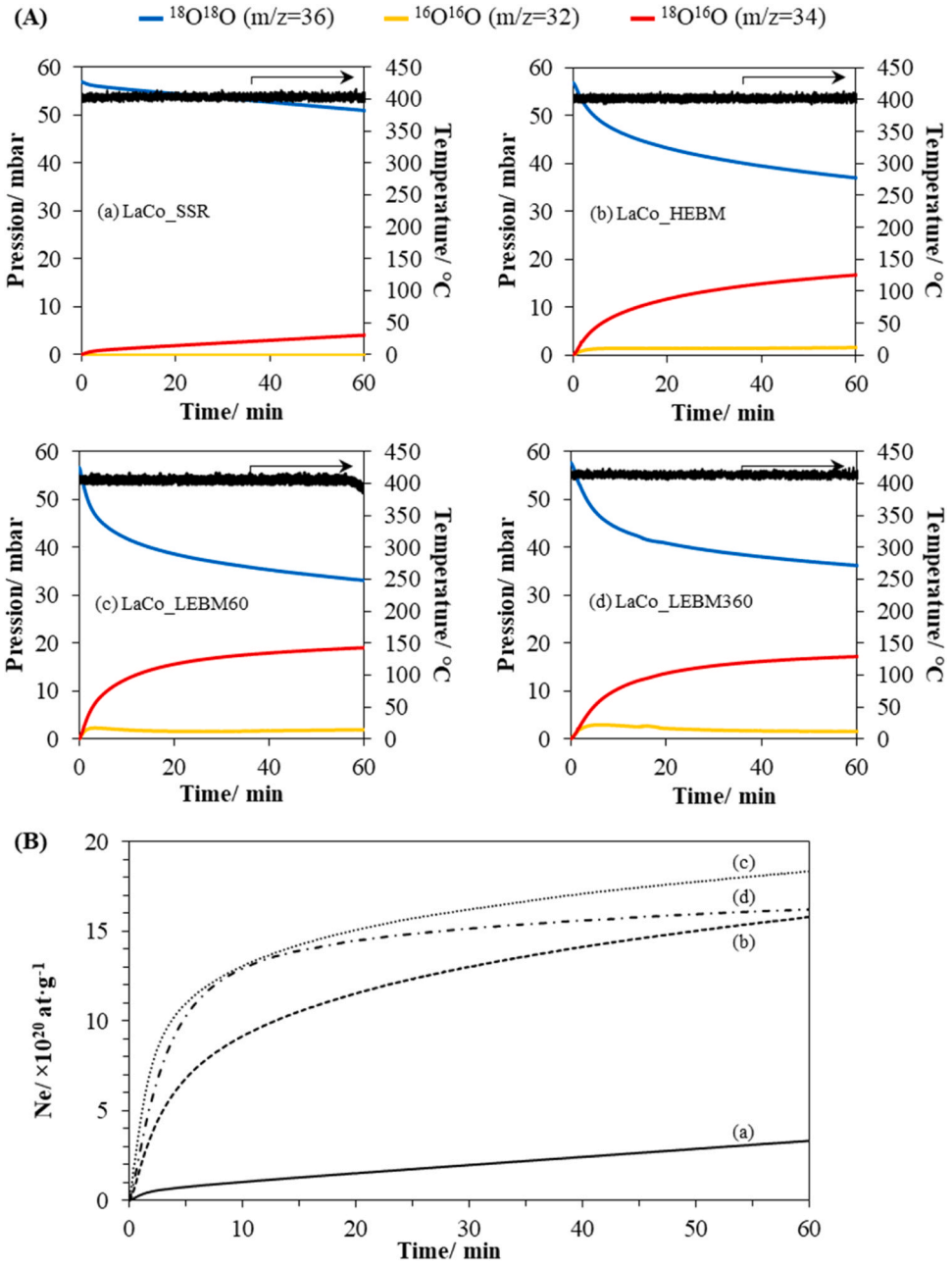

Fig. 7. Oxygen isotopic exchange experiments: (A) $^{18}O^{18}O$, $^{18}O^{16}O$, $^{16}O^{16}O$ dioxygen partial pressure evolution and (B) number of oxygen atoms exchanged over time for (a) LaCo_SSR, (b) LaCo_HEBM, (c) LaCo_LEBM60 and (d) LaCo_LEBM360 samples, at a constant temperature of 400 °C.

sample while being maximal for the LaCo_LEBM60 sample. This increase is explained by structural and textural properties changes that occur during both HEBM and LEBM processes, respectively with the formation of grain boundaries and SSA increase. Despite the low SSA of LaCo_-HEBM sample (3.5 $m^2 \cdot g^{-1}$), the large difference of activity observed for this sample compared with that measured for the LaCo_SSR sample confirms that the grain boundaries are the location of very high O diffusion as reported in [51]. The increase of the SSA favors the concentration of portholes for the adsorption of $^{18}O_2$ and desorption of $^{16}O^{18}O$ molecules which explains the high $V_{e,ini}$ value for LaCo_LEBM60. However, LaCo_LEBM360 sample shows a lower initial exchange rate than LaCo_LEBM60 sample despite having a much higher SSA value (Table 1). The lower oxygen mobility can be explained by Fe surface contamination that becomes more significant for extended grinding times. Royer et al. pointed out the negative effect of iron on oxygen mobility from $LaCo_{1-x}Fe_xO_3$ materials [51,53]: the higher the iron contamination, the lower the oxygen exchange rate. Therefore, a lower oxygen diffusion coefficient through $LaFeO_3$ material compared to the $LaCoO_3$ one was also reported by Nitadori et al. [54]. The evolution of the number of exchanged atoms after 60 min of reaction shows the same trend as initial exchange rate one but it can be seen that the curves converge towards the same value for all samples except LaCo_SSR (Table 3). This indicates that after 60 min of exchange in the recycling system, the fraction of exchange atoms is mainly dependent on the crystallite size which is roughly the same for LaCo_HEBM, LaCo_LEBM60 and LaCo_LEBM360 samples and limited to surface and sub-surface layers.

Isotopic exchange phenomenon is closely dependent to the temperature parameter, thus any direct comparison with literature should be handle with care. Nonetheless, LaCo_LEBM60 sample exhibits a SSA normalized initial exchange rate comparable to those obtained at 450 °C for bulk $LaCoO_3$ materials ($V_{e,ini}$ = 23.0 ×10^{17} at. $s^{-1} \cdot m^{-2}$) [55].

3.2. Catalytic performance

Catalytic performances of selected $LaCoO_3$ samples in the toluene total oxidation reaction are shown in Fig. 8(A). Toluene conversion into CO_2 was plotted as a function of temperature. The only detected products during reaction were CO_2 and H_2O and the carbon balance was around 100% along the whole catalytic run (Fig. A3.). T_{50} values (*i.e.* Temperature corresponding to a toluene conversion into CO_2 of 50%) are reported in Table 4. For comparison, Pt/Al_2O_3 catalyst performance was also evaluated as a reference (Fig. 8 (A)). As expected the catalytic activity of $0.5Pt/Al_2O_3$ was higher at low temperatures (160–220 °C) than that of $LaCoO_3$. However, at higher temperatures (>220 °C), the $LaCoO_3$ catalysts compared favorably with the reference catalyst.

Table 4
T_{50} values and kinetics data obtained from light-off curves.

Sample	T_{50} (°C)	a_{215} [a] ($mmol \cdot s^{-1} \cdot m^{-2}$)	Ea [b] ($kJ \cdot mol^{-1}$)	$A_{0\ corr}$ [c] (s^{-1})
LaCo_SSR	293	1.85×10^{-6}	152.7	2.3×10^{14}
LaCo_HEBM	227	1.73×10^{-5}	170.1	1.3×10^{16}
LaCo_LEBM60	213	3.24×10^{-5}	163.3	3.4×10^{16}
LaCo_LEBM120	216	8.14×10^{-6}	154.5	2.7×10^{16}
LaCo_LEBM360	221	3.15×10^{-6}	147.6	2.7×10^{16}

[a] activity determined at T = 215 °C;
[b] determined in the range $X(\%) < 20\%$;
[c] Extrapolated using the Ea average value.

The LaCo_SSR sample shows poor catalytic performances in the toluene total oxidation reaction with a conversion value of 63% at a temperature of 300 °C, while the sample ground at high energy (LaCo_HEBM) performs significantly better with a light-off curve shifted to the lower temperatures by ~65 °C (Fig. 8(A)). Samples from the low energy ball milling step (*i.e.* LaCo_LEBM30–360) show even higher catalytic activity. However, an extended LEBM grinding time leads to slightly decreased catalytic activity (*e.g.* LaCo_LEBM120 and LaCo_-LEBM360) (Table 4).

Based on their respective intrinsic activity, calculated at a temperature of 215 °C (a_{215}, Table 4), $LaCoO_3$ samples can be ranked as follow: LaCo_LEBM60 > LaCo_HEBM >> LaCo_LEBM120 >> LaCo_-LEBM360 > LaCo_SSR. Interestingly, activity evolution does not follow SSA increase (Table 1) but shows a similar trend with OIE results and exchange rate (Table 3).

Fig. 8(B) shows Arrhenius plots for conversion rate (X) lower than 20% to assume the chemical regime and considering a partial order of 1 and 0, respectively for toluene and oxygen [18]. Activation energies (Ea) extracted from Arrhenius plots are ranging from 147.6 to 170.1 $kJ \cdot mol^{-1}$ (Table 4) which are slightly higher than those obtained for $LaMnO_{3.15}$ et $LaFeO_3$ catalysts in identical conditions (Ea = 126–164 $kJ \cdot mol^{-1}$) [29] or Pecchi *et al.* $La_{1-x}Ca_xBO_3$ (B = Fe, Ni) catalysts (Ea = 100–153 $kJ \cdot mol^{-1}$) [56].

Corrected pre-exponential factors ($A_{0\ corr}$) were recalculated considering an average activation energy (Ea) of 159 $kJ \cdot mol^{-1}$ (Table 4) and its evolution as a function of catalysts SSA values is presented in Fig. 8(C). In the first part of the curve, the $A_{0\ corr}$ increases along with the SSA values to reach a maximum with the LaCo_LEBM60 sample. For higher SSA values, $A_{0\ corr}$ tends to slightly decrease. This behavior is mostly explained by two antagonist phenomena which are: (i) the SSA increase and thus, the active sites number increase; (ii) the surface enrichment with iron during grinding process, acting as a poisoning agent. The Fe contamination cannot be ignored since the benefit of the

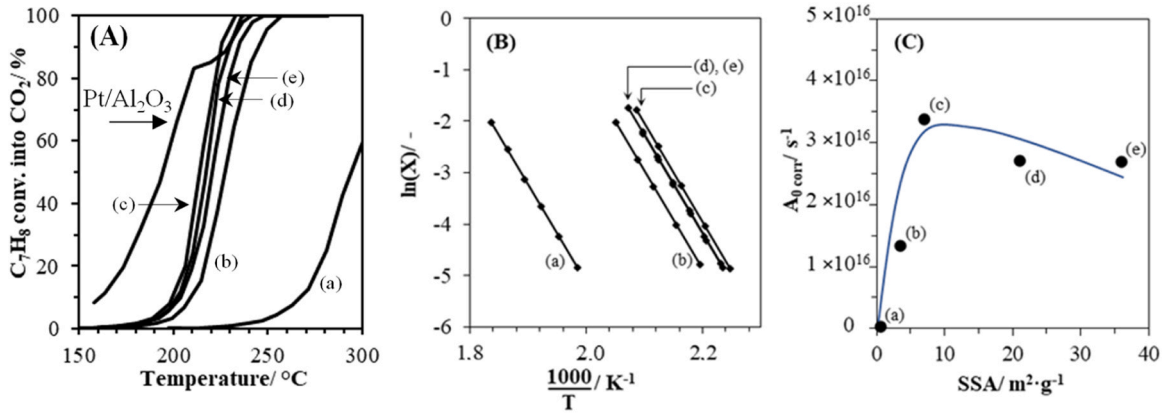

Fig. 8. (A) Light-off curves and corresponding (B) Arrhenius plots (X < 20%) and (C) evolution of corrected pre-exponential factors with catalyst surface area, obtained for the toluene total oxidation reaction over $LaCoO_3$ samples: (a) SSR, (b) HEBM, (c) LEBM60, (d) LEBM120 and (e) LEBM360 and over $0.5Pt/Al_2O_3$ (reference catalyst). Conditions: 200 mg of catalyst, 100 $mL \cdot min^{-1}$ of 1000 ppmv C_7H_8 in synthetic air (20% O_2 in N_2).

SSA increase over $A_{0\ corr}$ is overwhelmed by the impact of increasing Fe concentration for prolonged grinding time (*e.g.* LaCo_LEBM120 et LaCo_LEBM360) (Table 1, Fig. 3(C)). In addition, the negative impact of highly iron contaminated samples in formaldehyde, methane and carbon monoxide has been reported [17,28].

Table 5 reports results from the literature for $LaCoO_3$ catalysts developed for the total oxidation of toluene under catalytic test conditions similar to those used in this work. On the basis of T_{50}, it can be emphasized that the catalytic performance of ball-milled $LaCoO_3$ is very close to those of $LaCoO_3$ catalysts reported in the literature (Table 5).

Catalyst stability experiments are performed at a constant temperature of 220 °C, for a duration of 70 h in dry conditions, similar to the catalytic test ones (Fig. 9). Both catalysts show a rapid deactivation within the first five hours of the reaction which is explained by their stabilization in reaction, due most probably to the existence of a transient period before the quasi-stationary state is reached. The activity of LaCo_HEBM catalyst is quite stable for the next 65 h, while the activity of the LaCo_LEBM120 catalyst continues to monotonously decrease. The LaCo_LEBM120 catalyst was also tested over a longer period (100 h) at a temperature of 230 °C. As expected, the initial conversion is higher (82%) compared with the same catalyst tested at 220 °C (65%) (Fig. 9). As observed at 220 °C, the activity of the LaCo_LEBM120 catalyst decreased monotonically with time, until a conversion of 70% was achieved after 100 h of testing. LaCo_HEBM and LaCo_LEBM120 catalysts express comparable activity coefficient a_{220} values (see experimental section) with respectively 0.70 and 0.69. Used LaCo_LEBM120 catalyst after 70 h of testing does not show any textural, structural nor surface major modification.

In order to mimic real conditions, catalytic performance of the LaCo_LEBM120 catalyst for the toluene total oxidation reaction are also evaluated in wet conditions. Toluene conversion into CO_2 curves are showed in Fig. 10 for a RH at 20 °C up to 75%. No activity loss is observed under low relative humidity values (0–25%) while a negative impact is observed for higher RH values (+50%). Such behavior is commonly seen in the oxidation reaction of hydrocarbon molecules in wet conditions [57–61]. This diminution in catalytic activity can be explained by a water-toluene adsorption competitive mechanism [57]. The following reactional path underlines these adsorption phenomena (steps (1) and (2)):

$$H_2O_{(g)} + * \rightleftarrows H_2O_{(ads)} \quad (3)$$

$$C_7H_{8(g)} + * \rightleftarrows C_7H_{8(ads)} \quad (4)$$

$$C_7H_{8(ads)} + 9O_2 \longrightarrow 7CO_{2(ads)} + 4H_2O_{(ads)} \quad (5)$$

$$CO_{2(ads)} \rightleftarrows CO_{2(g)} + * \quad (6)$$

$$H_2O_{(ads)} \rightleftarrows H_2O_{(g)} + * \quad (7)$$

In addition, the desorption of water molecules (step (5)) is disadvantaged in presence of water in gas feed, obstructing the vicinity of active sites.

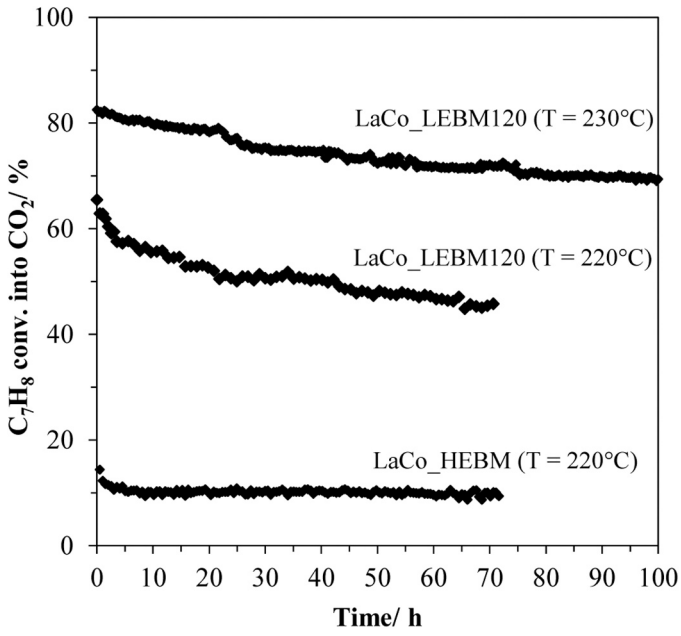

Fig. 9. Stability experiments for LaCo_HEBM and LaCo_LEBM120 samples. Conditions: 200 mg of catalyst exposed to 1000 ppmv C_7H_8 in to 100 mL·min^{-1} of synthetic air (20% O_2 in N_2) for 70 h and 100 h at a constant temperature.

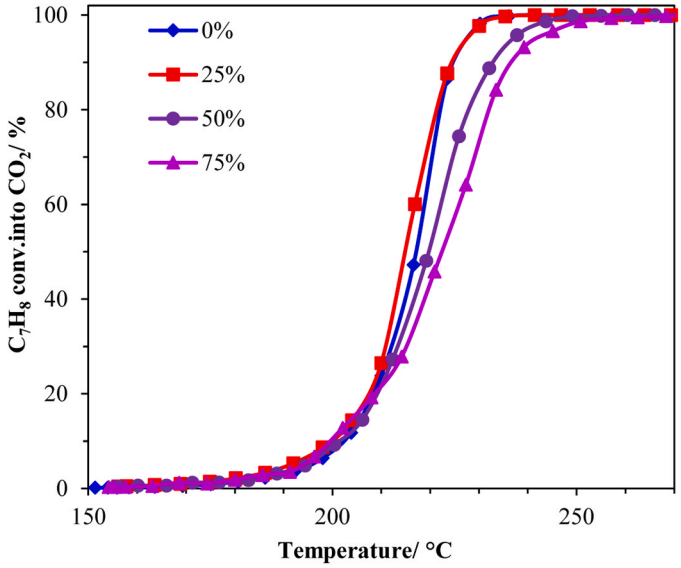

Fig. 10. Light-off curves obtained for the toluene total oxidation reaction over the LaCo_LEBM120 sample in wet conditions. Conditions: 200 mg of catalyst exposed to 1000 ppmv C_7H_8 in to 100 mL·min^{-1} of synthetic air (20% O_2 in N_2) and a relative humidity ranging from 0 to 75% at 20 °C.

Table 5
Literature survey of catalytic oxidation of toluene in the presence of $LaCoO_3$ and in the presence of $Pt(0.5\%)/Al_2O_3$ (Reference) with similar operating conditions of testing.

Catalysts	Studied effect	[Toluene] / ppm	WHSV / mL g^{-1} h^{-1}	T_{50} / °C	Reference
$LaCoO_3$ LEBM120	Ball milling	1000	30,000	216	This work
$LaCoO_3$	Spin states of Co^{3+}	500	60,000	210	[31]
$LaCoO_3$	Acetic acid treatment	1000	60,000	206	[32]
$LaCoO_3$	A-site nonstoichiometric	1000	60,000	212	[33]
$0.5Pt/Al_2O_3$	Reference	1000	30,000	194	This work

4. Conclusions

$LaCoO_3$ perovskites were successfully obtained using a top-down three steps reactive grinding process, followed by a final 400 °C calcination step for 3 h for thermal stabilization. Physical and chemical properties of synthesized materials were significantly impacted at each step of the reactive grinding sequence. The solid-state reaction step resulted in the formation of well crystallized $LaCoO_3$ perovskite material, whereas both high and low energy ball milling steps respectively achieved a mean crystal size decrease to a nanometric scale (about 11 to 13 nm) and specific surface area improvement (up to 50 $m^2 \cdot g^{-1}$ before final calcination). Iron contamination from grinding elements was detected, the major Fe amount being brought along the LEBM step, and found to increase linearly with grinding time. In addition, material recovery parameters from the LEBM step (*i.e.* perovskite residence time in water) could lead to undesirable secondary phases and thus, artificially high SSA values. Cobalt reducibility was much more modified over the HEBM step than the LEBM one because of crystals fractioning. Enhanced oxygen availability along reactive grinding process was evidenced by oxygen desorption and oxygen isotopic exchange experiments. Nonetheless, extended LEBM grinding time resulted a negative impact on oxygen availability which was correlated with significant iron contamination. Catalytic performances were improved after each step of reactive grinding (SSR < HEBM < LEBM) with a maximum found for a LEBM grinding time of 60 min, exceeding this value resulted in reduced catalytic performances despite catalysts exhibiting higher specific surface area values. The addition of water in the stream had no impact over catalytic activity until a relative humidity of 25% where a drop occurred above this concentration. During long term stability test, $LaCoO_3$ catalysts showed a pronounced deactivation in the early reaction period (0–5 h) then slowly monotonously decreased.

CRediT authorship contribution statement

Heidinger Bertrand: Investigation, Visualization, Writing – original draft. **Royer Sébastien:** Conceptualization, Methodology, Supervision, Writing – review & editing, Formal analysis. **Giraudon Jean-Marc:** Conceptualization, Formal analysis, Writing – review & editing. **Alamdari Houshang:** Conceptualization, Funding acquisition, Project administration, Supervision, Writing – review & editing. **Lamonier Jean-Francois:** Conceptualization, Data curation, Project administration, Supervision, Validation, Writing – review & editing. **Simon Pardis:** Investigation, Writing – review & editing. **Bion Nicolas:** Investigation, Writing – review & editing.

Declaration of Competing Interest

The authors declare that they have no known competing financial interests or personal relationships that could have appeared to influence the work reported in this paper.

Data Availability

Data will be made available on request.

Acknowledgements

This research is supported by a European Program INTERREG V France-Wallonie-Flanders (FEDER) (DepollutAir). The Chevreul Institute is thanked for its help in the development of this work through the ARCHI-CM project supported by the "Ministère de l'Enseignement Supérieur de la Recherche et de l'Innovation", the region "Hauts-de-France", the ERDF program of the European Union and the "Métropole Européenne de Lille". The authors thank Olivier Gardoll and Laurence Burylo for their contribution in H_2-TPR/O_2-TPD and XRD measurements, respectively.

Appendix A. Supporting information

Supplementary data associated with this article can be found in the online version at doi:10.1016/j.jece.2024.112107.

References

[1] Publications office of the European Union website. European Union emission inventory report 1990–2018 under the UNECE Convention on Long-range Transboundary Air Pollution (LRTAP). Available online: https://op.europa.eu/s/pb1d (accessed on 6 March 2019). https://doi.org/10.2800/233574
[2] M. Amann, M. Lutz, The revision of the air quality legislation in the European Union related to ground-level ozone, J. Hazard. Mater. 78 (2000) 41–62, https://doi.org/10.1016/S0304-3894(00)00216-8.
[3] C. He, J. Cheng, X. Zhang, M. Douthwaite, S. Pattisson, Z. Hao, Recent advances in the catalytic oxidation of volatile organic compounds: a review based on pollutant sorts and sources, Chem. Rev. 119 (2019) 4471–4568, https://doi.org/10.1021/acs.chemrev.8b00408.
[4] J.M. Donald, K. Hooper, C. Hopenhayn-Rich, Reproductive and developmental toxicity of toluene: a review, Environ. Health Perspect. 94 (1991) 237–244, https://doi.org/10.1289/ehp.94-1567945.
[5] J.F. Hamilton, P.J. Webb, A.C. Lewis, M.M. Reviejo, Quantifying small molecules in secondary organic aerosol formed during the photo-oxidation of toluene with hydroxyl radicals, Atmos. Environ. 39 (2005) 7263–7275, https://doi.org/10.1016/j.atmosenv.2005.09.006.
[6] F.G. Shahna, F. Golbabaei, J. Hamedi, H. Mahjub, H.R. Darabi, S.J. Shahtaheri, Treatment of benzene, toluene and xylene contaminated air in a bioactive foam emulsion reactor, Chin. J. Chem. Eng. 18 (2010) 113–121, https://doi.org/10.1016/S1004-9541(08)60331-6.
[7] Eur-LEX European Union Law website. Official Journal of the European Union, Commission Directive 2006/15/EC. Available online: https://eurlex.europa.eu/eli/dir/2006/15/oj (accessed on 6 March 2019)
[8] B. Lou, N. Shakoor, M. Adeel, P. Zhang, L. Huang, Y. Zhao, W. Zhao, Y. Jiang, Y. Rui, Catalytic oxidation of volatile organic compounds by non-noble metal catalyst: current advancement and future prospectives, J. Clean. Prod. 363 (2022) 132523, https://doi.org/10.1016/j.jclepro.2022.132523.
[9] V. Brummer, S.Y. Teng, D. Jecha, P. Skryja, V. Vavrcikova, P. Stehlik, Contribution to cleaner production from the point of view of VOC emissions abatement: a review, J. Clean. Prod. 361 (2022) 132112, https://doi.org/10.1016/j.jclepro.2022.132112.
[10] N. Lin, Y. Gong, R. Wang, Y. Wang, X. Zhang, Critical review of perovskite-based materials in advanced oxidation system for wastewater treatment: Design, applications and mechanisms, J. Hazard. Mater. 424 (2022) 127637, https://doi.org/10.1016/j.jhazmat.2021.127637.
[11] T. Nitadori, T. Ichiki, M. Misono, Catalytic properties of perovskite-type mixed oxides (ABO3) consisting of rare earth and 3d transition metals. The roles of the A- and B-site ions, Bull. Chem. Soc. Jpn. 61 (1988) 621–626, https://doi.org/10.1246/bcsj.61.621.
[12] S. Royer, D. Duprez, Catalytic oxidation of carbon monoxide over transition metal oxides, ChemCatChem 3 (2011) 24–65, https://doi.org/10.1002/cctc.201000378.
[13] S. Royer, D. Duprez, F. Can, X. Courtois, C. Batiot-Dupeyrat, S. Laassiri, H. Alamdari, Perovskites as substitutes of noble metals for heterogeneous catalysis: dream or reality, Chem. Rev. 114 (2014) 10292–10368, https://doi.org/10.1021/cr500032a.
[14] M. Wu, S. Ma, S. Chen, W. Xiang, Y. Yu, Fe-O terminated LaFeO3 perovskite oxide surface for low temperature toluene oxidation, J. Clean. Prod. 277 (2020) 123224, https://doi.org/10.1016/j.jclepro.2020.123224.
[15] Johnson Matthey website. PGM Market Report. Available online: http://platinum.matthey.com/ (accessed on 03 April 2023)
[16] L. Wachowski, Influence of the method of preparation on the porous structure of perovskite oxides, Surf. Coat. Technol. 29 (1986) 303–311, https://doi.org/10.1016/0257-8972(86)90003-4.
[17] S. Royer, F. Bérubé, S. Kaliaguine, Effect of the synthesis conditions on the redox and catalytic properties in oxidation reactions of LaCo1-xFexO3, Appl. Catal. A Gen. 282 (2005) 273–284, https://doi.org/10.1016/j.apcata.2004.12.018.
[18] C. Zhang, Y. Guo, Y. Guo, G. Lu, A. Boreave, L. Retailleau, A. Baylet, A. Giroir-Fendler, $LaMnO_3$ perovskite oxides prepared by different methods for catalytic oxidation of toluene, Appl. Catal. B Environ. 148–149 (2014) 490–498, https://doi.org/10.1016/j.apcatb.2013.11.030.
[19] Y. Liu, H. Dai, J. Deng, L. Zhang, Z. Zhao, X. Li, Y. Wang, S. Xie, H. Yang, G. Guo, Controlled generation of uniform spherical $LaMnO_3$, $LaCoO_3$, Mn_2O_3, and Co_3O_4 nanoparticles and their high catalytic performance for carbon monoxide and toluene oxidation, Inorg. Chem. 52 (2013) 8665–8676, https://doi.org/10.1021/ic400832h.
[20] W. Si, Y. Wang, S. Zhao, F. Hu, J. Li, A Facile Method for in Situ Preparation of the MnO_2/$LaMnO_3$ Catalyst for the Removal of Toluene, Environ. Sci. Technol. 50 (2016) 4572–4578, https://doi.org/10.1021/acs.est.5b06255.
[21] P. Courty, H. Ajot, C. Marcilly, B. Delmon, Oxydes mixtes ou en solution solide sous forme très divisée obtenus par décomposition thermique de précurseurs amorphes, Powder Technol. 7 (1973) 21–38, https://doi.org/10.1016/0032-5910(73)80005-1.
[22] Y. Luo, J. Zuo, X. Feng, Q. Qian, Y. Zheng, D. Lin, B. Huang, Q. Chen, Good interaction between well dispersed Pt and LaCoO3 nanorods achieved rapid Co3+/

Co2+ redox cycle for total propane oxidation, Chem. Eng. J. 357 (2019) 395–403, https://doi.org/10.1016/j.cej.2018.09.158.
[23] P. Baláž, M. Achimovîcová, M. Baláž, P. Billik, Z. Cherkezova-Zheleva, J. Manuel Criado, F. Delogu, E. Dutková, E. Gaffet, F.José Gotor, R. Kumar, I. Mitov, T. Rojac, M. Senna, A. Streletskii, K. Wieczorek-Ciurowa, Hallmarks of mechanochemistry: from nanoparticles to technology, Chem. Soc. Rev. 42 (2013) 7571–7637, https://doi.org/10.1039/C3CS35468G.
[24] H. Alamdari, S. Royer, Chapter 2: Mechanochemistry, in: P. Granger, V. I. Parvulescu, W. Prellier (Eds.), Perovskites and Related Mixed Oxides, Wiley-VCH Verlag GmbH & Co. KGaA, Weinheim, Germany, 2015, pp. 25–46, https://doi.org/10.1002/9783527686605.ch02.
[25] Qiwu Zhang, Fumio Saito, Mechanochemical synthesis of $LaMnO_3$ from La_2O_3 and Mn_2O_3 powders, J. Alloy. Compd. 297 (2000) 99–103, https://doi.org/10.1016/S0925-8388(99)00606-4.
[26] S. Kaliaguine, A. Van Neste, V. Szabo, J.E. Gallot, M. Bassir, R. Muzychuk, Perovskite-type oxides synthesized by reactive grinding: Part I. Preparation and characterization, Appl. Catal. A. Gen. 209 (2001) 345–358, https://doi.org/10.1016/S0926-860X(00)00779-1.
[27] B. Levasseur, S. Kaliaguine, Methanol oxidation on $LaBO_3$ (B = Co, Mn, Fe) perovskite-type catalysts prepared by reactive grinding, Appl. Catal. A Gen. 343 (2008) 29–38, https://doi.org/10.1016/j.apcata.2008.03.016.
[28] C. Ciotonea, R. Averlant, G. Rochard, A.S. Mamede, J.M. Giraudon, H. Alamdari, J.-F. Lamonier, S. Royer, A simple and green procedure to prepare efficient manganese oxide nanopowder for the low temperature removal of formaldehyde, ChemCatChem 9 (2017) 2366–2376, https://doi.org/10.1002/cctc.201700199.
[29] B. Heidinger, S. Royer, H. Alamdari, J.-M. Giraudon, J.-F. Lamonier, Reactive grinding synthesis of $LaBO_3$ (B: Mn, Fe) perovskite; properties for toluene total oxidation, Catalysts 9 (2019) 633, https://doi.org/10.3390/catal9080633.
[30] S. Laassiri, N. Bion, D. Duprez, S. Royer, H. Alamdari, Clear microstructure–performance relationships in Mn-containing perovskite and hexaaluminate compounds prepared by activated reactive synthesis, Phys. Chem. Chem. Phys. 16 (2014) 4050–4060, https://doi.org/10.1039/C3CP54363C.
[31] H. Chen, P. Liu, P., G. Wei, Y. Huang, X. Lin, X. Liang, J. Zhu, Effect of electron structure on the catalytic activity of $LaCoO_3$ perovskite towards toluene oxidation, Chem. Commun. 58 (30) (2022) 4731–4734, https://doi.org/10.1039/D2CC00404F.
[32] Q. Yang, D. Wang, C. Wang, X. Li, K. Li, Y. Peng, J. Li, Facile surface improvement method for LaCoO3 for toluene oxidation, Catal. Sci. Technol. 8 (2018) 3166–3173, https://doi.org/10.1039/C8CY00765A.
[33] A. Zhao, Y. Ren, H. Wang, Z. Qu, Enhancement of toluene oxidation performance over $La_{1-x}CoO_{3-\delta}$ perovskite by lanthanum non-stoichiometry, J. Environ. Sci. 127 (2023) 811–823, https://doi.org/10.1016/j.jes.2022.06.042.
[34] M. Ghasdi, H. Alamdari, S. Royer, A. Adnot, Electrical and CO gas sensing properties of nanostructured $La_{1-x}Ce_xCoO_3$ perovskite prepared by activated reactive synthesis, Sens. Actuators B Chem. 156 (2011) 147–155, https://doi.org/10.1016/j.snb.2011.04.003.
[35] S. Irusta, M.P. Pina, M. Menéndez, J. Santamaria, Catalytic combustion of volatile organic compounds over la-based perovskites, J. Catal. 179 (1998) 400–412, https://doi.org/10.1006/jcat.1998.2244.
[36] C. Zhang, C. Wang, W. Zhan, Y. Guo, Y. Guo, G. Lu, A. Baylet, A. Giroir-Fendler, Catalytic oxidation of vinyl chloride emission over $LaMnO_3$ and $LaB_{0.2}Mn_{0.8}O_3$ (B = Co, Ni, Fe) catalysts, Appl. Catal. B Environ. 129 (2013) 509–516, https://doi.org/10.1016/j.apcatb.2012.09.056.
[37] R. Hammami, S.Ben Aïssa, H. Batis, Effects of thermal treatment on physico-chemical and catalytic properties of lanthanum manganite LaMnO3+y, Appl. Catal. A Gen. 353 (2009) 145–153, https://doi.org/10.1016/j.apcata.2008.10.048.
[38] J. Deng, L. Zhang, H. Dai, H. He, C.T. Au, Strontium-doped lanthanum cobaltite and manganite: highly active catalysts for toluene complete oxidation, Ind. Eng. Chem. Res. 47 (2008) 8175–8183, https://doi.org/10.1021/ie800585x.
[39] J.L.G. Fierro, L. Gonzalez Tejuca, Non-stoichiometric surface behavior of $LaMO_3$ oxides as evidenced by XPS, Appl. Surf. Sci. 27 (1987) 453–457, https://doi.org/10.1016/0169-4332(87)90154-1.
[40] J.L.G. Fierro, Structure and composition of perovskite surface in relation to adsorption and catalytic properties, Catal. Today 8 (1990) 153–174, https://doi.org/10.1016/0920-5861(90)87016-V.
[41] N.S. Mc Intyre, M.G. Cook, X-ray photoelectron studies on some oxides and hydroxides of cobalt, nickel, and copper, Anal. Chem. 47 (1975) 2208–2213, https://doi.org/10.1021/ac60363a034.
[42] J. Yang, H. Liu, W.N. Martens, R.L. Frost, Synthesis and characterization of cobalt hydroxide, cobalt oxyhydroxide, and cobalt oxide nanodiscs, J. Phys. Chem. C. 114 (2010) 111–119, https://doi.org/10.1021/jp908548f.
[43] M.C. Biesinger, B.P. Payne, A.P. Grosvenor, L.W.M. Lau, A.R. Gerson, R. St.C. Smart, Resolving surface chemical states in XPS analysis of first row transition metals, oxides and hydroxides: Cr, Mn, Fe, Co and Ni, Appl. Surf. Sci. 257 (2011) 2717–2730, https://doi.org/10.1016/j.apsusc.2010.10.051.
[44] Y. Wu, C. Cordier, E. Berrier, N. Nuns, C. Dujardin, P. Granger, Surface reconstructions of $LaCo_{1-x}Fe_xO_3$ at high temperature during N_2O decomposition in realistic exhaust gas composition: impact on the catalytic properties, Appl. Catal. B Environ. 140–141 (2013) 151–163, https://doi.org/10.1016/j.apcatb.2013.04.002.
[45] M. Futai, C. Yonghua, L. Hangzhou, Characterization of perovskite-type oxide catalysts $RECoO_3$ by TPR, React. Kinet. Catal. Lett. 31 (1986) 47–53, https://doi.org/10.1007/BF02062510.
[46] L. Simonot, F. Garin, G. Maire, A comparative study of $LaCoO_3$, Co_3O_4 and $LaCoO_3$-Co_3O_4 I. Preparation, characterisation and catalytic properties for the oxidation of CO, Appl. Catal. B Environ. 11 (1997) 167–179, https://doi.org/10.1016/S0926-3373(96)00046-X.
[47] J. Faye, A. Baylet, M. Trentesaux, S. Royer, F. Dumeignil, D. Duprez, S. Valange, J.-M. Tatibouët, Influence of lanthanum stoichiometry in $La_{1-x}FeO_{3-\delta}$ perovskites on their structure and catalytic performance in CH_4 total oxidation, Appl. Catal. B Environ. 126 (2012) 134–143, https://doi.org/10.1016/j.apcatb.2012.07.001.
[48] J.A. Marcos, R.H. Buitrago, E.A. Lombardo, Surface chemistry and catalytic activity of $La_{1-y}M_yCoO_3$ perovskite (M = Sr or Th): 1. Bulk and surface reduction studies, J. Cat. 105 (1987) 95–106, https://doi.org/10.1016/0021-9517(87)90011-X.
[49] L. Lisi, G. Bagnasco, P. Ciambelli, S. De Rossi, P. Porta, G. Russo, M. Turco, Perovskite-type oxides: II. Redox properties of $LaMn_{1-x}Cu_xO_3$ and $LaCo_{1-x}Cu_xO_3$ and methane catalytic combustion, J. Solid State Chem. 146 (1999) 176–183, https://doi.org/10.1006/jssc.1999.8327.
[50] D. Ferri, L. Forni, Methane combustion on some perovskite-like mixed oxides, Appl. Catal. B Environ. 16 (1998) 119–126, https://doi.org/10.1016/S0926-3373(97)00065-9.
[51] S. Royer, D. Duprez, S. Kaliaguine, Oxygen mobility in $LaCoO_3$ perovskites, Catal. Today 112 (2006) 99–102, https://doi.org/10.1016/j.cattod.2005.11.020.
[52] M. Richard, F. Can, S. Gil, A. Giroir-Fendler, D. Duprez, N. Bion, Study of lanthanum manganate and yttrium-stabilized zirconia-supported palladium dual-bed catalyst system for the total oxidation of methane: a study by 18O2/16O2 isotopic exchange, ChemCatChem 8 (2016) 1921–1928, https://doi.org/10.1002/cctc.201501398.
[53] S. Royer, D. Duprez, S. Kaliaguine, Role of bulk and grain boundary oxygen mobility in the catalytic oxidation activity of $LaCo_{1-x}Fe_xO_3$, J. Catal. 234 (2005) 364–375, https://doi.org/10.1016/j.jcat.2004.11.041.
[54] T. Nitadori, M. Misono, Catalytic properties of $La_{1-x}A'_xFeO_3$ (A′ = Sr, Ce) and $La_{1-x}Ce_xCoO_3$, J. Catal 93 (1985) 459–466, https://doi.org/10.1016/0021-9517(85)90193-9.
[55] M. Bonne, N. Bion, F. Pailloux, S. Valange, S. Royer, J.M. Tatibouët, D. Duprez, Improved oxygen mobility in nanosized mixed-oxide particles synthesized using a simple nanocasting route, Chem. Commun. 37 (2008) 4504–4506, https://doi.org/10.1039/B808699K.
[56] G. Pecchi, M.G. Jiliberto, E.J. Delgado, L.E. Cadús, J.L.G. Fierro, Effect of B-site cation on the catalytic activity of La1−xCaxBO3 (B = Fe, Ni) perovskite-type oxides for toluene combustion, J. Chem. Technol. Biotechnol. 86 (2011) 1067–1073, https://doi.org/10.1002/jctb.2611.
[57] H.Y. Pan, M.Y. Xu, Z. Li, S.S. Huang, C. He, Catalytic combustion of styrene over copper based catalyst: Inhibitory effect of water vapor, Chemosphere 76 (2009) 721–726, https://doi.org/10.1016/j.chemosphere.2009.04.019.
[58] R. Kikuchi, S. Maeda, K. Sasaki, S. Wennerström, K. Eguchi, Low-temperature methane oxidation over oxide-supported Pd catalysts: inhibitory effect of water vapor, Appl. Catal. Gen. 232 (2002) 23–28, https://doi.org/10.1016/S0926-860X(02)00096-0.
[59] C. Lahousse, A. Bernier, P. Grange, B. Delmon, P. Papaefthimiou, T. Ioannides, X. Verykios, Evaluation of γ-MnO_2 as a VOC removal catalyst: comparison with a noble metal catalyst, J. Catal. 178 (1998) 214–225, https://doi.org/10.1006/jcat.1998.2148.
[60] X. Li, L. Wang, Q. Xia, Z. Liu, Z. Li, Catalytic oxidation of toluene over copper and manganese based catalysts: effect of water vapor, Catal. Commun. 14 (2011) 15–19, https://doi.org/10.1016/j.catcom.2011.07.003.
[61] J. Hu, W.B. Li, R.F. Liu, Highly efficient copper-doped manganese oxide nanorod catalysts derived from CuMnO hierarchical nanowire for catalytic combustion of VOCs, Catal. Today 314 (2018) 147–153, https://doi.org/10.1016/j.cattod.2018.02.009.